Oceanic redox condition during the late Ediacaran (551–541 Ma), South China

Haifeng Fan [a,c,*], Hanjie Wen [a,b], Tao Han [a], Xiangkun Zhu [c],
Lianjun Feng [d], Huajin Chang [e]

[a] State Key Laboratory of Ore Deposit Geochemistry, Institute of Geochemistry, Chinese Academy of Sciences, Guiyang 550081, China
[b] University of Chinese Academy of Sciences, Beijing 100049, China
[c] MNR Key Laboratory of Deep-Earth Dynamics, MNR Key Laboratory of Isotope Geology, Institute of Geology, Chinese Academy of Geological Sciences, Beijing 100037, China
[d] Institute of Geology and Geophysics, Chinese Academy of Sciences, Beijing 100029, China
[e] School of Geosciences, Hubei University of Arts and Sciences, Xiangyang 441053, China

Abstract

The late Ediacaran (551–541 Ma) oceanic environment could represent a significant preparation for the enrichment of redox sensitive elements during the early Cambrian and even for the evolution of life. However, the marine environment during the late Ediacaran has not been thoroughly characterized to date. To better understand late Ediacaran oceanic redox conditions, we investigated the Fe and S isotopic compositions of cherts from the slope (Yinjiang) and basin (Silikou) sections of the Nanhua basin in South China. The slope (Yinjiang) section is characterized by a wide range of $\delta^{56}Fe_T$ values ($-0.12‰$ to $1.06‰$) and by continuously decreasing $\delta^{34}S_{Py}$ values from $40.4‰$ to $4.1‰$. The variable $\delta^{56}Fe_T$ values in the Yinjiang section primarily reflect the various oxidation degrees of dissolved Fe^{2+} in ferruginous seawater. The homogeneous $\delta^{56}Fe_T$ signatures ($0.02–0.40‰$) along the Silikou section and the decreasing trend of $\delta^{56}Fe_{HR}$ values from $0.86‰$ to near zero primarily depend on the mixing of Fe^{3+} hydroxide/oxide precipitates in a ferruginous water column, possibly followed by partial reduction, the authigenic framboidal pyrite trapped within an intermittent euxinic condition and detrital silicate Fe minerals. A 20–30‰ discrepancy in $\delta^{34}S_{Py}$ values between the Yinjiang and Silikou sections may be ascribed to the formation of diagenetic pyrites and framboidal pyrites, respectively. Therefore, the continuously decreasing $\delta^{34}S_{Py}$ values in the Yinjiang and Silikou sections may reflect a significant increase of sulfate diffusion into sediments at the slope location and the enlarged marine sulfate reservoir at the basin location. These new results indicate that the deep water in the Nanhua basin is primarily characterized by a ferruginous condition with intermittent euxinic conditions in the basin location during the late Ediacaran.
© 2018 Elsevier Ltd. All rights reserved.

Keywords: Late Ediacaran Ocean; Fe and S isotopes; Ferruginous condition; Intermittent euxinia

1. INTRODUCTION

A number of redox proxies have suggested an increasing oxygen level in deep water during the early Ediacaran (635–551 Ma) (Fike et al., 2006; Canfield et al., 2007; Scott et al., 2008; Sahoo et al., 2012; Kendall et al., 2015). However, a redox-stratified oceanic model (oxic surface water and ferruginous deep water, occasionally with a euxinic wedge or

* Corresponding author at: State Key Laboratory of Ore Deposit Geochemistry, Institute of Geochemistry, Chinese Academy of Sciences, Guiyang 550081, China.
  E-mail address: fanhaifeng@mail.gyig.ac.cn (H. Fan).

euxinic deep water) has also been suggested (Canfield et al., 2008; Li et al., 2010; Han and Fan, 2015; Kurzweil et al., 2015). Recently, the existence of a modern-like ocean during the early Cambrian, where there may have been completely oxic deep water with an oxygen minimum zone (OMZ), has been proposed based on Mo isotopes (Wen et al., 2015; Chen et al., 2015b). If that proposal is true, then the late Ediacaran (551–541 Ma) ocean may represent a fundamental transition of the oceanic redox condition away from the redox-stratified model of the early Ediacaran and toward the modern-like model of the early Cambrian. However, other publications have argued that the early Cambrian ocean remained anoxic and exhibited a high degree of redox heterogeneity (e.g., Sperling et al., 2015; Jin et al., 2016; Li et al., 2017). In this circumstance, the oxygen levels of the ocean and atmosphere during the late Ediacaran could only show a modest increase (e.g., Sperling et al., 2015; Huang et al., 2018). In addition, the evolution of life from immobile animals with soft and flexible tissues during the Ediacaran to the complex organisms with mineralized skeletons characteristic of the early Cambrian (Knoll and Carroll, 1999; Zhu et al., 2007) could be related to the oceanic redox condition of the late Ediacaran (e.g., Sperling et al., 2015).

Unfortunately, the late Ediacaran (551–541 Ma) oceanic redox condition is not well understood, despite the fact that several studies have been carried out attempting to resolve this issue (e.g., Halverson and Hurtgen, 2007; Fike and Grotzinger, 2008; Cui et al., 2016). For instance, previous studies have suggested a dominant ferruginous deep-water condition in the Nanhua basin based on Fe speciation analysis of cherts in the Liuchapo/Laobao/Piyuancun Formations (Canfield et al., 2008; Chang et al., 2010a; Wang et al., 2012; Xiang et al., 2017). However, Fe speciation analysis was originally estimated from Fe mineral species in clastic sediments, including modern oxic and euxinic clay and shales, Phanerozoic shale, mudstone, and middle Proterozoic black shale (e.g., Canfield et al., 1996; Raiswell et al., 1988; Poulton and Raiswell, 2002; Raiswell et al., 2001; Shen et al., 2002). Therefore, the utility of this method, using sediments poor in clastic particles and total Fe, should be carefully considered (Lyons et al., 2012). Recently, the applicability of the Fe speciation method to estimate carbonate was calibrated by Clarkson et al. (2014), who proposed that a total Fe content of <0.5% commonly provides suspiciously high Fe_{HR}/Fe_T ratios (>0.38, up to 1.0). One can doubt that the Fe speciation method may be a risky proxy with which to identify the paleo-depositional redox condition of the late Ediacaran chert with total Fe < 0.5%.

The Fe and S isotopic fractionations are strongly sensitive to changes in oceanic redox conditions, which have been widely applied without considering the lithology of the sediments. Moreover, recrystallization during burial should not affect the composition of bulk rock, even though it may redistribute isotopes between individual mineral phases (Kunzmann et al., 2017). Therefore, the coupling of Fe and S isotopes has been recently used to trace the redox evolution of Earth's surface conditions (e.g.,

Marin-Carbonne et al., 2014; Kurzweil et al., 2015; Eickmann et al., 2018). To better constrain the late Ediacaran oceanic redox condition, both slope and basin sections of the Nanhua basin in South China were chosen for this study, which investigated the Fe and S isotopic compositions and the Fe speciation of late Ediacaran sedimentary sequences.

2. GEOLOGICAL SETTING

The Nanhua basin was located between the Yangtze and Cathaysia tectonic blocks (Fig. 1, Wang and Li, 2003). During the late Ediacaran, the shallow water deposits of the Yangtze Platform were represented by the Dengying Formation dolostones. In the slope and basin setting of the Nanhua basin, abundant cherts are widely distributed (e.g., Chen et al., 2009, 2015a). These chert sequences, with thicknesses of up to 100 m in the deeper basin, are known as the Liuchapo Formation at the slope locations in Guizhou and Hunan Provinces and as the Laobao Formation at the basin locations in the Guangxi Zhuang Autonomous Region. In this study, both the slope (Yinjiang) and basin (Silikou) sections were investigated (Fig. 1).

The Yinjiang section (N 27°57′32″, E 108°35′42″) is located in the northeastern part of Guizhou Province, including the Ediacaran Doushantuo Formation (dolostone and black shale), the Liuchapo Formation (gray-black laminated chert), and the Cambrian Jiumenchong Formation (black shale) along the upwards outcrop (Fig. 2, Fan et al., 2013), and all of them represent slope deposition. The thickness of the Liuchapo Formation is approximately 40 m. The Liuchapo Formation chert displays variable crystal sizes of quartz, from several microns to several hundred microns (Fan et al., 2013). The median $\delta^{30}Si$ value (+0.2‰ to +0.7‰) indicates the mixing of a silicon source from ambient seawater, continental clastic materials, and even hydrothermal fluid (Fan et al., 2013).

The Silikou section (N 25°44′27″, E 109°30′43″) is located in the Silikou village of Sanjiang Dong Autonomous County in the northern part of the Guangxi Zhuang Autonomous Region. This section comprises the Ediacaran Doushantuo Formation (siltstone), the Laobao Formation (black-gray chert), and the lower Cambrian Qingxi Formation (black shale) from bottom to top, and all of them represent basin deposition (Fig. 1, Chang et al., 2010a, b, 2012). The Laobao Formation is approximately 169 m in thickness and consists of black thick-bedded chert in the lower part and dark-gray chert bands with carbonaceous or siliceous mudstone interbeds in the upper part (Fig. 2). The Laobao Formation chert shows finely laminated fabrics and cryptocrystalline or microcrystalline structures without metasomatic relict textures or distinct recrystallization (Chang et al., 2010a). Near-modern seawater Ge/Si ratios (0.4–0.5 μmol/mol) and rare earth element patterns suggest a normal seawater silicon source, rather than a hydrothermal fluid source (Chang et al., 2010b; Dong et al., 2015).

The Liuchapo/Laobao Formation is generally a diachronous stratigraphic unit (e.g., Wang et al., 2012; Chen
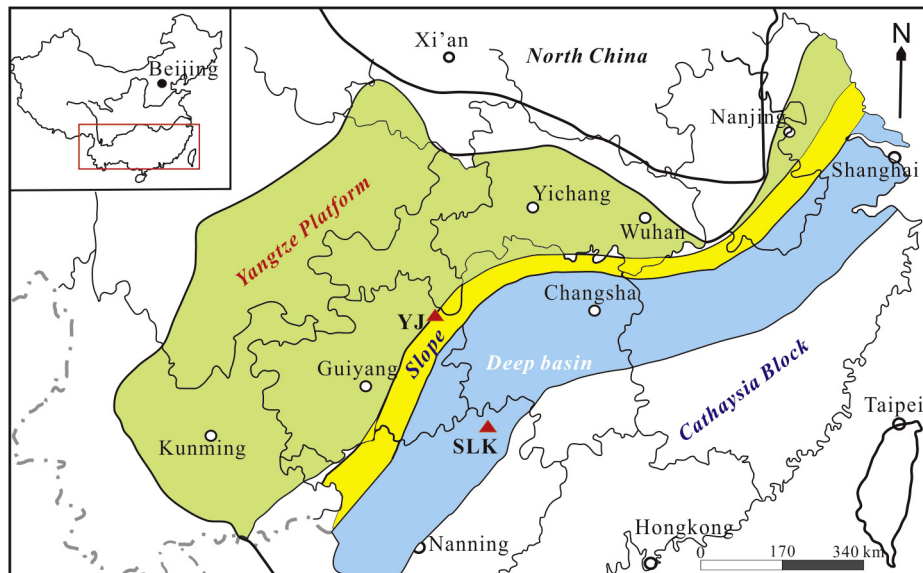
Fig. 1. Simplified paleogeographic map of the Yangtze Platform in South China during the Ediacaran to Early Cambrian, showing three sedimentary facies (platform, slope, and basin) and the locations of the Yinjiang (YJ) and Silikou (SLK) sections studied (triangles) in this study.
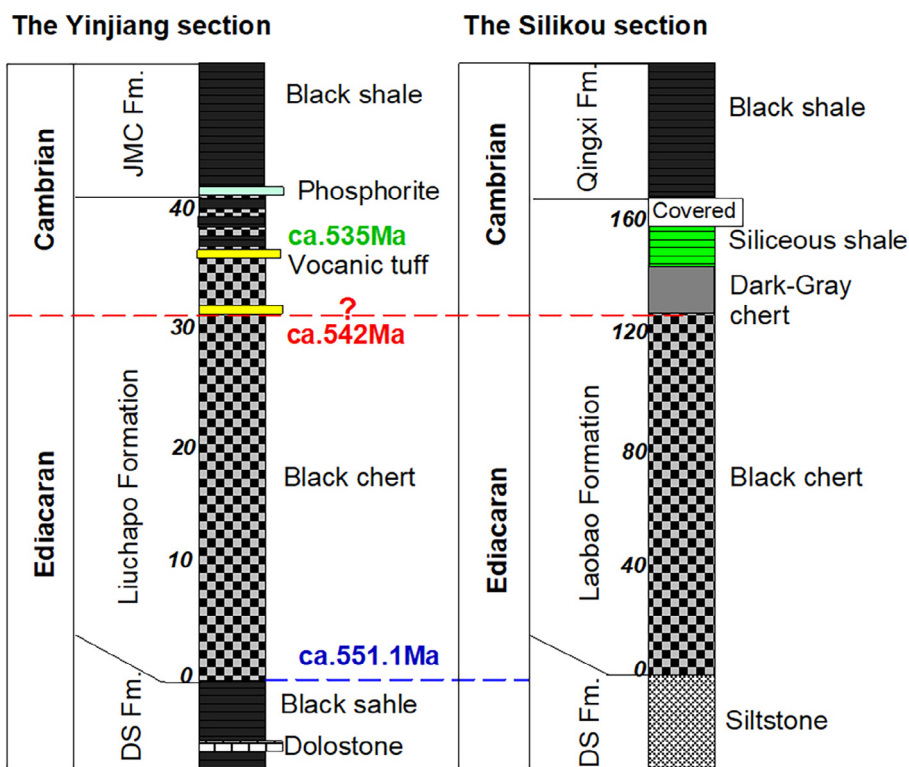

Fig. 2. Lithology and stratigraphic profiles of the Yinjiang and Silikou sections, modified from Chang et al. (2012), Fan et al. (2013), and Dong et al. (2015). DS Fm. = Doushantuo Formation, JMC Fm. = Jiumenchong Formation.

et al., 2015a). Recently, Chen et al. (2015a) reported two new SIMS U-Pb zircon ages of 541.1 ± 5.0 Ma and 541.6 ± 3.7 Ma in the middle-upper Liuchapo Formation from eastern Guizhou Province (30 km to the Yinjiang section), which directly indicated the Ediacaran-Cambrian boundary within the Liuchapo (slope) and Laobao (basin) Formations (Fig. 2). The top of the Liuchapo/Laobao Formation can be correlated to the middle Zhongyicun Member (~535.2 ± 1.7 Ma) of the Meishucun Formation (Zhu et al., 2009; Yang et al., 2017), whereas the bottom

boundary of the Liuchapo/Laobao Formation can be related to that of the Dengying Formation with an age of $\sim551.1 \pm 0.7$ Ma (Condon et al., 2005; Yang et al., 2017).

3. ANALYTICAL METHODS

3.1. 1 Iron isotopes

All samples were ashed at 500 °C to remove organic material before digestion. Approximately 200-mg powder samples were weighed in a beaker and digested using an acid mixture of ultrapure HF and HNO_3 at 120 °C. After the evaporation of HF and HNO_3, the samples were diluted in 2 ml 6 N HCl. The clear solution was loaded on AMPG-1 resin to purify iron, following the method described by Zhu et al. (2002) and Tang et al. (2006). The recoveries were always better than 98%. Total Fe concentrations and Fe isotopic ratios were measured using a Nu-MC-ICP-MS at the Institute of Geology, Chinese Academy of Geological Sciences, following the techniques described by Zhu et al. (2008). The Fe isotopic results were expressed in the standard notation as $\delta^{56}Fe$ deviation from IRMM-014. International reference materials (BHVO-1 and BCR-2) and a Chinese standard (GSR-3) were measured together with our samples to monitor the accuracy of the method. The external long-term reproducibility (2σ) for $\delta^{56}Fe$ measurements using this method was better than ±0.10‰ (Zhao et al., 2012; Fan et al., 2014). The results of the reference materials were also consistent with those of previous studies (Appendix Table A.1).

3.2. Fe speciation and sulfur isotopes of pyrite

The Fe speciation and S isotopes of pyrite were measured at the State Key Laboratory of Biogeology and Environmental Geology, China University of Geosciences (Wuhan), following published methods (Poulton and Canfield, 2005; Li et al., 2015). The highly reactive Fe (Fe_{HR}) contains carbonate-associated Fe (Fe_{car}), ferric oxides (Fe_{ox}), magnetite (Fe_{mag}), and pyrite (Fe_{Py}). Then, Fe_{car}, Fe_{ox}, and Fe_{mag} concentrations were determined by Atomic Absorption Spectrometry (AAS) after being sequentially extracted by a sodium acetate solution, a sodium dithionite solution, and an ammonium oxalate solution. Additionally, Fe_{Py} was calculated from pyrite sulfur, which was extracted by using the $CrCl_2$ reduction method and precipitated as Ag_2S in silver nitrate traps (Canfield et al., 1986). The sulfur isotopic compositions of pyrites ($\delta^{34}S_{Py}$) were analyzed using a continuous flow isotope ratio mass spectrometer. All of the $\delta^{34}S$ values were reported against Vienna Canon Diablo Troilite (VCDT). The analytical precision for $\delta^{34}S$ was better than ±0.1‰. In this study, Fe species have only been used to estimate the proportion of different Fe-bearing minerals and not to trace redox conditions in the water column because the Fe species proxy was constructed from modern and ancient fine-grained siliciclastic marine sediments.

4. RESULTS

Iron mainly occurs as Fe oxides and diagenetic cubic pyrite in the Yinjiang cherts. In the middle of the section (11.5–26.5 m), more cubic pyrites (up to 1.14%) are observed surrounding barites (Fig. 3A). At the base and at the top of the section, a number of detrital silicates (feldspar), diagenetic cubic pyrites, and a few phosphate minerals are observed (Fig. 3B). The total Fe concentration of these cherts changes from 0.21% to 1.86% (Appendix Table A.1). The Fe_{HR}/Fe_T ratios in all of the samples change from 0.86 to 1.16, with Fe_{Py}/Fe_{HR} values between 0.02 and 0.74 (Fig. 4 and Appendix Table A.1). The major Fe-bearing minerals in the Silikou chert include Fe-oxides, framboidal pyrites, and detrital silicate Fe. The samples below 40 m mainly contain Fe-oxides and detrital silicate Fe (Fig. 3C and D). Most samples above 40 m contain a number of framboidal pyrites (Fig. 3E). It is also noted that more detrital silicates, monazites, and barites are present in the chert above 120 m (Fig. 3F).

The $\delta^{56}Fe_T$ values of the Yinjiang chert yield a range from -0.12‰ to 1.06‰ (Fig. 4 and Appendix Table A.1), and mostly between 0.25‰ and 0.56‰ (n = 10), with an average of 0.44‰ for all of the samples. Three cherts (Z_2l-86, 90, and 95) show higher $\delta^{56}Fe_T$ values from 0.80‰ to 1.06‰, and two samples (Z_2l-94 and 102) exhibit near-zero $\delta^{56}Fe_T$ values. The $\delta^{34}S_{Py}$ values of the Yinjiang chert yield a wide range from 4.1‰ to 40.4‰. The highest value (40.4‰) is preserved in the lower part of the section and continuously decreases to 4.1‰ in the upward direction (Fig. 4). In contrast, the Silikou chert exhibits a narrow range of $\delta^{56}Fe_T$ values from 0.02‰ to 0.40‰, with an average of 0.25‰ (Fig. 5 and Appendix Table A.1).

5. DISCUSSION

5.1. Fe isotope geochemistry

5.1.1. Partial oxidation of Fe^{2+} at the slope location (Yinjiang)

In a modern oxic seawater column, dissolved Fe^{2+} is completely oxidized to Fe^{3+} hydroxide/oxides, resulting in no net Fe isotope fractionation between Fe^{3+} hydroxide/oxides and seawater (Craddock and Dauphas, 2011; Li et al., 2013). In sediments, diagenetic pyrite commonly records $\delta^{56}Fe$ values similar to or lower than that of precursor Fe^{3+} hydroxide/oxides, which depend on the degree of Fe isotope fractionation during diagenesis (Severmann et al., 2008; Busigny et al., 2014; Sawaki et al., 2018). Nevertheless, the $\delta^{56}Fe$ values of the bulk sediments from the oxic condition are usually close to zero (e.g., Severmann et al., 2008; Fehr et al., 2010; Busigny et al., 2014). In oxygen-limited seawater, the partial oxidation of dissolved Fe^{2+} by a small quantity of oxygen and/or anoxygenic photosynthesis commonly enriches isotopically heavy Fe preferentially in the Fe^{3+} hydroxide/oxides, with variable $\Delta^{56}Fe_{oxide-Fe}^{2+}$ from 0.9‰ to 3.0‰ (e.g., Bullen et al., 2001; Johnson et al., 2002; Welch et al., 2003; Beard and Johnson, 2004; Beard et al., 2010). As a result, the $\delta^{56}Fe$
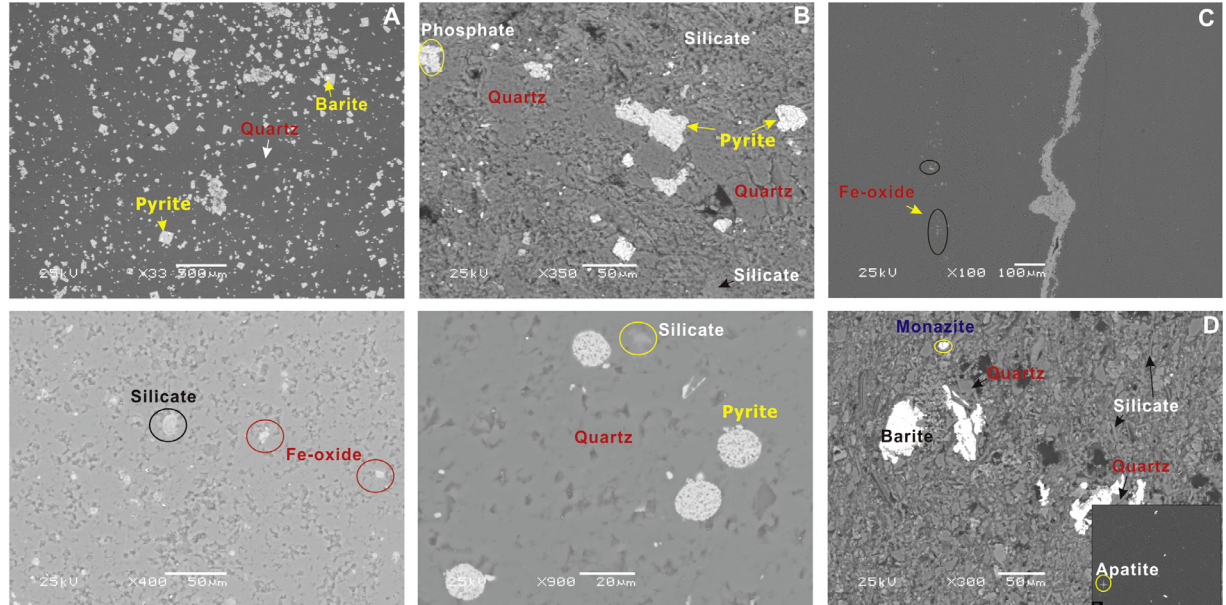
Fig. 3. A and B. Scanning electron microscopy (SEM) photomicrographs of the major minerals in the Yinjiang chert. Abundant cubic pyrites surrounding barite occur in the middle chert between the 13 m to 26.5 m location (Z_2l-109) (A). More silicate minerals and a few phosphate minerals are present in the top chert (Z_2l-109 at 40 m location) (B). (C–F) Scanning electron microscopy (SEM) photomicrographs of the major minerals in the Silikou chert. The samples below 40 m mainly contain Fe oxide and silicate Fe (C, D). The framboidal pyrites and few silicate minerals are observed in most cherts (E). The mean diameters of framboidal pyrite cluster are less than 5 μm for the samples below 80 m and approximately 6.5 μm for the upper samples above 93 m (Chang et al., 2009). More silicate minerals, monazites, and barites occur in the cherts above 120 m (F).
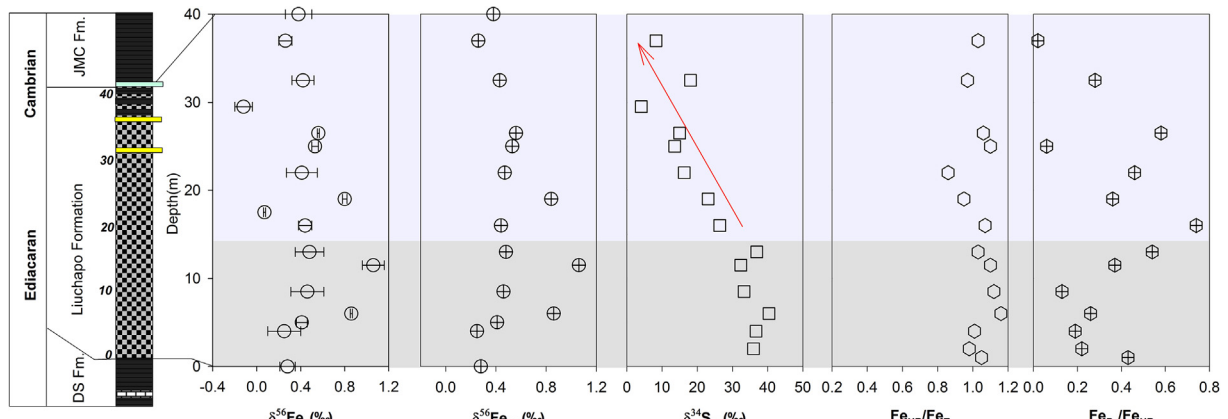

Fig. 4. Vertical variations of Fe and S isotopic compositions and Fe speciation along the Yinjiang section. The $\delta^{56}Fe_T$ values range from -0.12 to 1.06‰, without any systematic variation along the upwards section. The $\delta^{56}Fe_{HR}$ values of samples with Fe_{HR}/Fe_T ratios lower than 1.0 were calculated following a simple mass balance equation: $\delta^{56}Fe_T = Fe_{HR}/Fe_T * \delta^{56}Fe_{HR} + (1 - Fe_{HR}/Fe_T) * \delta^{56}Fe_{Detrital}$, where $\delta^{56}Fe_{Detrital}$ is a near-zero $\delta^{56}Fe$ value (∼0.05‰, Beard et al., 2003). Additionally, the $\delta^{56}Fe_{HR}$ values of the samples with $Fe_{HR}/Fe_T \geq 1.0$ are represented by $\delta^{56}Fe_T$ values. The samples below 13 m exhibit the homogenous $\delta^{34}S_{Py}$ (32.4–40.4‰) and the upper samples above 13 m are characterized by the $\delta^{34}S_{Py}$ values continuously decreasing from 26.4‰ to 4.1‰. The Fe_{HR}/Fe_T ratios are much closer to one and do not show any obvious change. However, the Fe_{Py}/Fe_{HR} ratios show a wide range from 0.02 and 0.74, but with a chief peak in the 13 m to 26.5 m range.

values of bulk sediments from an oxygen-depleted and ferruginous environment are usually more positive than those in water columns due to Fe^{3+} hydroxide/oxide precipitation (e.g., Johnson et al., 2003; Czaja et al., 2013; Li et al., 2013; Satkoski et al., 2015). For diagenetic pyrite, widely variable $\delta^{56}Fe$ values can be observed, ranging from negative to positive. These depend on the $\delta^{56}Fe$ values of the precursor

Fe^{3+} hydroxide/oxides, the extent of the reduction of Fe^{3+} hydroxide/oxides, and the availability of reduced ferrous iron at pyrite formations (Johnson et al., 2008; Nishizawa et al., 2010; Yoshiya et al., 2012; Sawaki et al., 2018). The quantitative reduction of Fe-oxide may increase $\delta^{56}Fe_{py}$ up to that of Fe-oxides; but the partial reduction gives a wide range of $\delta^{56}Fe_{py}$ values.
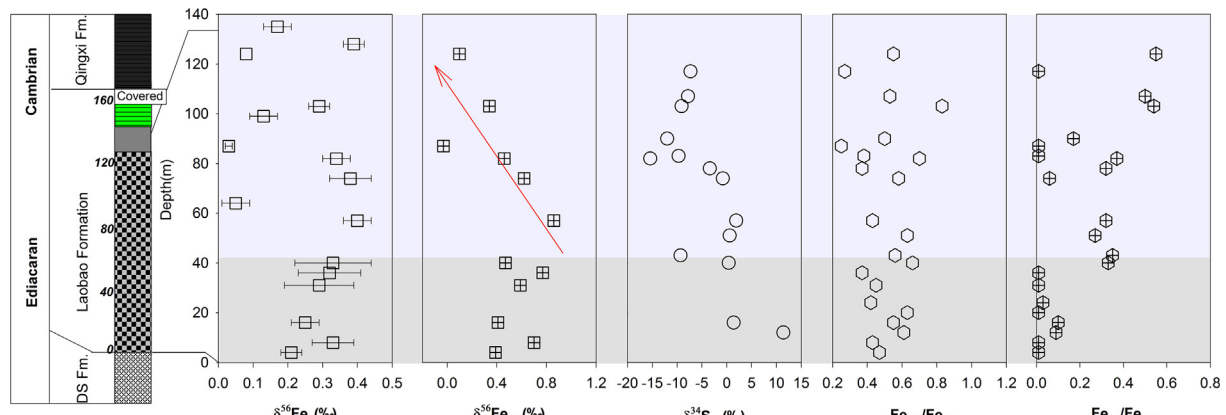
Fig. 5. Vertical variations in Fe and S isotopic compositions and Fe speciation of the Silikou section. The $\delta^{56}Fe_{HR}$ values were also calculated following a simple mass balance equation: $\delta^{56}Fe_T = Fe_{HR}/Fe_T * \delta^{56}Fe_{HR} + (1 - Fe_{HR}/Fe_T) * \delta^{56}Fe_{Detrital}$. The $\delta^{56}Fe_T$ do not show obvious variation, mostly between 0.03‰ and 0.40‰. The $\delta^{56}Fe_{HR}$ values are decreasing along the section above 40 m. The $\delta^{34}S_{Py}$ values show a wide range from 11.40‰ to −15.4‰, with a broadly decreasing curve along the upwards section. Samples below 40 m show very low Fe_{Py}/Fe_{HR} ratios and variable Fe_{HR}/Fe_T ratios (0.37–0.66). Samples above 40 m mostly exhibit wider range Fe_{HR}/Fe_T ratios (0.25–0.83) and higher Fe_{Py}/Fe_{HR} ratios (up to 0.55). The $\delta^{34}S_{Py}$ values and Fe speciation data are cited from Chang et al. (2010a, 2012).

The mixing of different Fe-bearing minerals has limited influence on the $\delta^{56}Fe_T$ values in the Yinjiang section. The Fe_{HR}/Fe_T ratios of these cherts are close to 1 (Appendix Table A.1 and Fig. 4), which indicates the absence of detrital Fe silicate minerals in these cherts. Therefore, the $\delta^{56}Fe_T$ of these cherts could mainly represent the signatures of highly reactive Fe, in which 70–90% of highly reactive Fe is present as Fe-oxide and pyrite. In addition, the cubic morphology of pyrite in these cherts indicates a diagenetic origin of pyrite through the precursor Fe^{3+} hydroxide/oxides (Fig. 3). Hence, we suggest that the $\delta^{56}Fe_T$ values may represent that of initially precipitated Fe-oxide, and can reflect ambient seawater redox conditions, rather than the mixing of different Fe-bearing minerals.

The positive $\delta^{56}Fe_T$ values of most Yinjiang cherts are similar to those of the Archean low-Fe chert (0.28–0.63‰) with high Fe/Th ratios deposited from ferruginous seawater (e.g., Li et al., 2013; Satkoski et al., 2015). These authors have proposed a significant and extensive partial oxidation of dissolved Fe^{2+} during the deposition of those shallow-water low-Fe cherts. At the redox chemocline, there occurs the partial oxidation of dissolved Fe^{2+}, which may result in the enrichment of isotopically heavy Fe in initial Fe^{3+} hydroxide/oxides. This mechanism has also been used to explain the positive $\delta^{56}Fe$ values of the Datangpo Formation shales (Zhang et al., 2015), the Doushantuo Formation cherts, pyrites in South China (Fan et al., 2014; Sawaki et al., 2018), and Neoproterozoic marine shales (Kunzmann et al., 2017). This partial oxidation may explain the positive $\delta^{56}Fe_T$ values of those samples with much more abundant cubic pyrite (e.g., Z_2l-100, 93, 91, 90). In these samples, the cubic pyrites formed through the reductive dissolution of the precursor Fe^{3+} hydroxide/oxides during early diagenesis. Therefore, to enrich isotopically heavy Fe in these pyrite-rich samples, the partial oxidation of dissolved Fe^{2+} is necessary in a ferruginous water column.

Nevertheless, the partial reduction of Fe^{3+} hydroxide/oxides to dissolved Fe^{2+} might be another potential mech-

anism for interpreting these positive $\delta^{56}Fe$ values. In modern anoxic lakes (e.g., the Black Sea) and OMZs in the upwelling area of Peru, slightly heavier Fe isotope compositions ($0 < \delta^{56}Fe < 0.2‰$) and lower Fe_T/Al ratios (<0.5) were observed in anoxic/OMZ sediments than in oxic sediments ($\delta^{56}Fe = 0‰$, $Fe_T/Al = \sim0.5$) (Fig. 6, Severmann et al., 2006, 2008; Scholz et al., 2014a,b; Busigny et al., 2014). This difference was explained by the loss of the light Fe isotope during the partial reduction of Fe^{3+} hydroxide/oxides. Indeed, a portion of cherts (e.g., Z_2L-104, 99, 88, 84) with considerably less cubic pyrite (Fig. 4) show $\delta^{56}Fe_T$ values $>0.25‰$ and Fe_T/Al ratios <0.5, which could indicate the loss of isotopically light Fe through partial
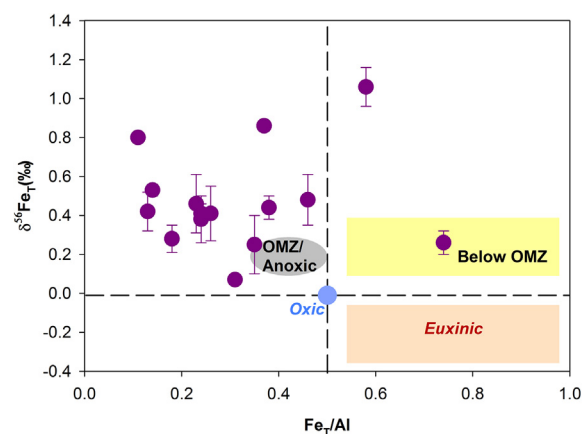
Fig. 6. Cross plot of $\delta^{56}Fe_T$ values versus Fe_T/Al ratios for cherts in the Yinjiang section, where samples with >1 Fe_T/Al ratios were not included. Modern sediments from oxic condition usually show near zero $\delta^{56}Fe_T$ values and ~0.5 Fe_T/Al ratios (Severmann et al., 2008; Scholz et al., 2014a,b). Sediments deposited within OMZs and/or anoxic areas commonly have $\delta^{56}Fe_T$ values of 0–0.2‰ and Fe_T/Al ratios < 0.5. Sediments in euxinic and/or below OMZ area exhibit Fe_T/Al ratios > 0.5 and $0‰ < \delta^{56}Fe_T < 0.4‰$.

reduction. However, the partial reduction of Fe^{3+} hydroxide/oxides might not significantly change the $\delta^{56}Fe_T$ values in bulk sediments, based on observations in modern anoxic basins and OMZs. Moreover, no clear negative correlation between $\delta^{56}Fe_T$ values and Fe_T/Al ratios was observed (Fig. 6). Therefore, the positive $\delta^{56}Fe_T$ values in the Yinjiang chert are considered to mainly reflect the degree of partial oxidation of dissolved Fe^{2+} in ferruginous water columns, with a minor loss of isotopically light Fe by partial reduction during diagenesis.

5.1.2. Mixing of different Fe-minerals at the basin location (Silikou section)

The occurrence of framboidal pyrites with 5–18 μm diameters in the Silikou chert has been reported by our coworkers (Chang et al., 2009, 2012). Framboidal pyrites are commonly formed in ferruginous and euxinic conditions (e.g., Wilkin et al., 1996). In a euxinic condition, framboidal pyrite were characterized by a mostly <5 μm diameter with a narrow size range because of their shorter growth times compared with those of pyrite formed within anoxic sediment porewaters underlying oxic water columns (Wilkin et al., 1996; Wignall and Newton, 1998). Under euxinic conditions, the dissolved Fe^{2+} reacts with reductive H_2S resulting from bacterial sulfate reduction as framboidal pyrite, in which the isotopically light Fe is preferentially enriched with variable fractionation factors ($\Delta^{56}Fe_{Dissolve\ Fe-Pyrite} = -0.3$ to 3.0‰, Butler et al., 2005; Guilbaud et al., 2011; Wu et al., 2012). Under such euxinic conditions, pyrites have $\delta^{56}Fe$ values similar to those of a water column when its dissolved Fe is quantitatively transformed into pyrite (Severmann et al., 2008). Under ferruginous conditions, authigenic pyrites (>5 μm) formed below the oxic-anoxic boundary in modern isolated lakes, and these pyrites usually did not preserve the $\delta^{56}Fe$ value of the overlying water and thus show variable but negative $\delta^{56}Fe$ values (Duan et al., 2010; Fehr et al., 2010; Busigny et al., 2014).

With the exception of framboidal pyrites, the Silikou cherts also contain Fe^{3+} hydroxide/oxides and detrital silicate Fe (Chang et al., 2010a). Iron isotopic compositions of highly reactive Fe (Fig. 5) were calculated using a simple mass balance equation: $\delta^{56}Fe_T = Fe_{HR}/Fe_T * \delta^{56}Fe_{HR} + (1 - Fe_{HR}/Fe_T)*\delta^{56}Fe_{Detrital}$, where $\delta^{56}Fe_{Detrital}$ has a near-zero $\delta^{56}Fe$ value (~0.05‰, Beard et al., 2003). Cherts from the basin location exhibit positive $\delta^{56}Fe_{HR}$ values mostly higher than 0.4‰, which may indicate the small extent of oxidation of dissolved Fe^{2+} and/or the partial reduction of the Fe^{3+} hydroxide/oxides into dissolved Fe^{2+} in a water column. It is well known that the partial oxidation of dissolved Fe^{2+} is a major mechanism for the extremely positive $\delta^{56}Fe$ values in Precambrian BIFs and cherts, although partial reduction during the dissimilatory process has also been suggested (e.g., Johnson et al., 2008; Czaja et al., 2013; Li et al., 2013; Satkoski et al., 2015). As mentioned above, partial oxidation occurred at the slope location (Yinjiang), which indicates that a redox chemocline may be present in the water column. Therefore, the positive and variable $\delta^{56}Fe_{HR}$ values (0.39–0.77‰) in the basin cherts (below 40 m) with low Fe_{Py}/Fe_T ratios

(0.01–0.10) may suggest a ferruginous condition, where dissolved Fe^{2+} was partially oxidized at a redox chemocline. Subsequently, broadly decreasing $\delta^{56}Fe_{HR}$ values, from 0.86‰ to −0.03‰, are observed above 40 m, which indicates that the dissolved Fe^{2+} with more negative $\delta^{56}Fe$ values may be more effectively captured by the enhanced H_2S in an intermittent euxinic condition at the sediment-water interface. It is noted that some cherts (e.g., SLK-57, 74, 82) in the upper part (43–82 m) show higher Fe_{Py}/Fe_T ratios (up to 0.37) but more positive $\delta^{56}Fe_{HR}$ values (0.46–0.86‰) than the other cherts (Fig. 5), which might indicate that a partial reduction of initial Fe^{3+} hydroxide/oxides occurred when they passed into an anoxic water column. However, no systematic correlation between $\delta^{56}Fe_{HR}$ values and pyrite/oxide content was observed in these cherts, which may be attributed to the Fe isotopic fractionation during partial oxidation, reduction, and the pyrite formation processes.

Here, we propose that Fe^{3+} hydroxide/oxides, formed through partial oxidation of dissolved Fe^{2+} at a redox chemocline, might be followed by partial reduction during their precipitation, during which isotopically heavy Fe was preserved in the residual Fe^{3+} hydroxide/oxides. Framboidal pyrites, formed through the precursor FeS_m phase at the water-sediment interface, enrich isotopically light Fe. The mixing of Fe^{3+} hydroxide/oxides and framboidal pyrites play an important role in regulating the $\delta^{56}Fe_{HR}$ signatures of these cherts at the Silikou section.

5.2. Decreasing trend of $\delta^{34}S_{Py}$ values

In the Yinjiang section, the $\delta^{34}S_{Py}$ values exhibit a continuously decreasing trend (Fig. 4). The cherts in the lower part (0–13 m) show relatively uniform $\delta^{34}S_{Py}$ values (32.4–40.4‰), which is consistent with those of pyrites in carbonate (549 Ma) from South China and Namibia (Ries et al., 2009; Cui et al., 2016). These positive $\delta^{34}S_{Py}$ values are also similar to those of contemporaneous marine sulfates associated with carbonates (40‰ in South China and Oman) (Fike and Grotzinger, 2008; Cui et al., 2016), which indicates no net sulfur isotope fractionation between the marine sulfate and pyrite. Given the pyrite morphology (cubic) (Fig. 3a and b) and low Fe_{Py}/Fe_T ratios (Appendix Table A.1), the pyrites in the Yinjiang chert could have formed during the early diagenesis (Shen et al., 2003), where the seawater-sediment interface resulted in low sulfate diffusion. During this diagenetic process, there is no net S isotopic fractionation when the buried sulfate is quantitatively reduced to pyrite through the bacterial sulfate reduction (BSR) process (Lyons et al., 2009). Previous studies have also indicated that the BSR process can produce no obvious S isotopic fractionation (<6‰) between pyrite and sulfate with an insufficient sulfate concentration (50–200 μM) (e.g., Canfield and Thamdrup, 1994; Canfield, 2001; Habicht et al., 2002; Canfield et al., 2010). Similarly, high $\delta^{34}S_{Py}$ values (34.1‰) of diagenetic pyrites in the Doushantuo Formation chert nodules have been reported, which was explained by low levels of sulfate concentration in Ediacaran seawater (Xiao et al., 2010). Therefore, both the low sulfate diffusion into sediments and the diagenetic process could have minimized the S isotopic fractionation.
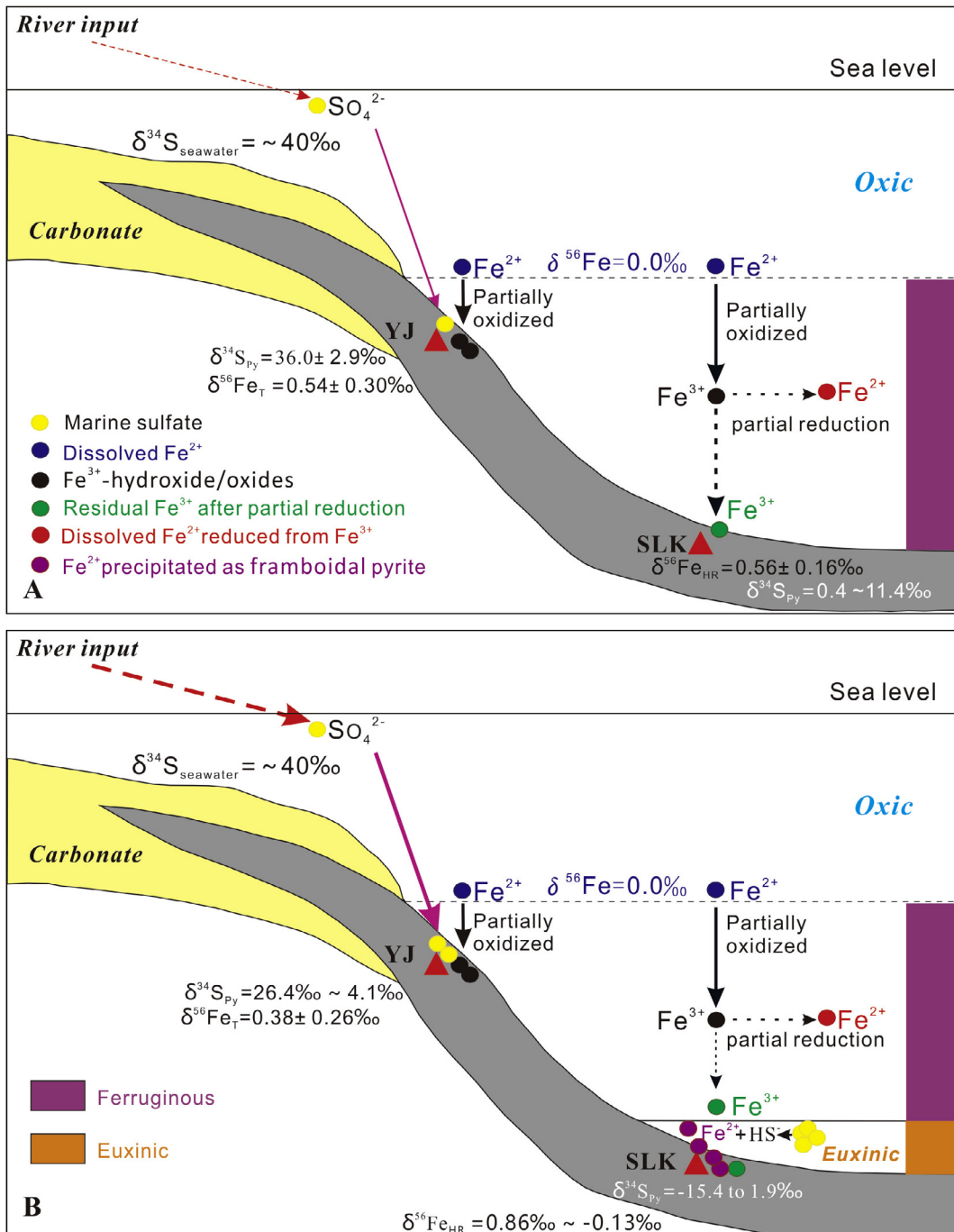
Fig. 7. Schematic diagram illustrating the redox condition of deep water in the Nanhua basin during the late Ediacaran. At the redox chemocline, dissolved Fe^{2+} was partially oxidized to Fe^{3+} hydroxide/oxides in a ferruginous water column, during which positive $\delta^{56}Fe$ values are preserved in the slope section (Yinjiang). The partial reduction of initial Fe^{3+} hydroxide/oxides may occur in a ferruginous water column before the initial Fe^{3+} hydroxide/oxides deposited at the basin location (Silikou), during which Fe^{3+} hydroxide/oxides deposited at the basin location may preserve more positive $\delta^{56}Fe$ values than that of the Yinjiang chert. At the first stage (Fig. 7A), burial sulfate was quantitatively reduced in sediments during early diagenesis at the Yinjiang section. However, sulfate reduction occurred in seawater column at the Silikou section. At the second stage (Fig. 7B), there is an increasing sulfate concentration at basin location and enhancing diffusion of sulfate into sediments at the slope location, which resulted in decreasing $\delta^{34}S_{Py}$ values along two investigated sections upwards. At the Silikou section, the reduction of sulfate may produce intermittent euxinic conditions, where dissolved Fe^{2+} are finally fixed as framboidal pyrites. The mixing of more framboidal pyrites with Fe^{3+} hydroxide/oxides could decrease the $\delta^{56}Fe_{HR}$ values from 0.86‰ to near zero. There is no significant change of redox condition along the two investigated upwards sections, although an intermittent euxinic condition occurred at the basin location.

Assuming a homogeneous sulfur isotope composition (40‰) of marine sulfate in the Nanhua basin, a large sulfur isotope fractionation ($\Delta^{34}S_{Sulfate-Pyrite}$ = 30–40‰) between framboidal pyrite and sulfate at the lower part of the Silikou location may suggest a sulfate-unlimited environment at the least.

If an invariable marine sulfate S isotope composition is assumed (∼40‰, Cui et al., 2016), then a decreasing $\delta^{34}S_{Py}$ trend could correspond to an increasing S isotope fractionation between sulfate and pyrite ($\Delta^{34}S_{Sulfate-Pyrite}$) from near zero to 30‰ in the Yinjiang section (Fig. 4). The same decreasing $\delta^{34}S_{Py}$ trend was reported at the basinal Silikou section (Fig. 5) and the platform Gaojiashan Formation in South China, and the Kotlim Formation in North Russia (Chang et al., 2012; Johnston et al., 2012; Cui et al., 2016). Although $\Delta^{34}S$ values depend on local depositional conditions such as sedimentation rate, sulfate reduction rate, and iron availability (Canfield, 2001 and references therein), they are largely controlled by the sulfate concentration during the BSR process (Habicht et al., 2002; Halverson and Hurtgen, 2007). When sulfate concentrations exceed 200 μM, large S isotope fractionation can occur during sulfate reduction (Habicht et al., 2002). The enhanced Fe_{Py}/Fe_{HR} ratios and decreasing $\delta^{34}S_{Py}$ trends during the transition from the lower to the upper part (Figs. 4 and 5) indicate the enhanced reduction of marine sulfate, which could correspond to an enlarged marine sulfate reservoir at the Silikou section (Chang et al., 2012) and to the enhanced diffusion of sulfate into the sediment at the Yinjiang section.

5.3. Implications for an oceanic redox condition during the late Ediacaran

Based on Fe and S isotopic variations, a spatial and temporal evolution model of the late Ediacaran oceanic redox condition with two stages is illustrated in Fig. 7. At the first stage, the variations of $\delta^{56}Fe_T$ values from 0.25‰ to 1.06‰ indicated that the Yinjiang chert was deposited in a ferruginous condition (probably near a redox chemocline), where dissolved Fe^{2+} was partially oxidized to Fe^{3+} hydroxide/oxides in the seawater column (Fig. 7A). In sediments, the initial Fe^{3+} hydroxide/oxides with positive $\delta^{56}Fe$ values precipitated from a ferruginous water column are partially reduced by organic carbon and/or Fe-reducing bacteria, which could result in the enrichment of isotopically heavy Fe in residual Fe^{3+} hydroxide/oxides and of light Fe isotopes in diagenetic pyrite. The changed Fe_{py}/Fe_{HR} ratios and stable $\delta^{34}S_{Py}$ values suggest that the buried sulfate was quantitatively reduced to H_2S through the BSR process, combined with reactive Fe^{2+}, and fixed as diagenetic cubic pyrite, which results in the seawater-like S isotopic signal in these cherts. The Fe^{3+} hydroxide/oxides in the Silikou chert may precipitate from the same redox chemocline as in the Yinjiang section, but a partial reduction of Fe^{3+} hydroxide/oxides might occur during precipitation in a ferruginous water column (Fig. 7A), resulting in the more positive $\delta^{56}Fe$ values in the residual Fe^{3+} hydroxide/oxides. Conversely, the reduction of dissolved sulfate occurred in a water column, where dissolved Fe^{2+} is not effectively

captured and precipitated as framboidal pyrite. However, a large sulfur isotope fractionation ($\Delta^{34}S_{Sulfate-Pyrite}$ = 30–40‰) at the Silikou section may suggest a sulfate-unlimited environment at the least.

The second stage might be best characterized by increasing marine sulfate concentration in the slope and basin locations (Fig. 7B). Accompanied by strong continental oxidative weathering, abundant dissolved sulfate was transported into the late Ediacaran ocean (Halverson and Hurtgen, 2007; Fike and Grotzinger, 2008; Cui et al., 2016). When sulfate flux in the late Ediacaran Ocean achieved a steady state, marine sulfate S isotopes could be maintained at a fixed value (Cui et al., 2016). During early diagenesis, the increasing diffusion of marine sulfate into sediments and partial sulfate reduction could control the decreasing $\delta^{34}S_{Py}$ values and the change in Fe_{Py}/Fe_{HR} ratios in the Yinjiang section. However, the Fe geochemical cycle did not show any obvious changes, while the $\delta^{56}Fe_T$ values from −0.12‰ to 0.80‰ reflect partial oxidation of dissolve Fe^{2+} near the redox chemocline (Fig. 7B). For the Silikou section, more marine sulfate was reduced to H_2S and then precipitated as framboidal pyrite, which resulted in high Fe_{Py}/Fe_{HR} ratios in some cherts and decreasing $\delta^{34}S_{Py}$, corresponding to an intermittent euxinic condition. The decreasing $\delta^{56}Fe_{HR}$ from 0.86‰ to near zero could indicate the mixing of more framboidal pyrite with Fe^{3+} hydroxide/oxides in the Silikou section (Fig. 7B).

Our new data provide evidence for redox stratified seawater during the late Ediacaran in South China, where the redox condition in the Yinjiang section is ferruginous and the Silikou section is characterized as ferruginous with intermittent euxinic water. However, no enrichment of redox sensitive elements (Mo, U, V) was observed in these two sections and in other reported sections (e.g., Chang et al., 2012; Sahoo et al., 2016; Xiang et al., 2017), which may suggest a limited redox sensitive element reservoir in the open ocean, if the Nanhua basin had been well-connected to the open ocean during the late Ediacaran.

6. CONCLUSIONS

This study contributes to the field by obtaining the $\delta^{56}Fe_T$ and $\delta^{34}S_{Py}$ values of cherts in the slope (Yinjiang) and basin (Silikou) sections from the Yangtze Platform in South China. The positive $\delta^{56}Fe_T$ values of the Yinjiang section reflect ferruginous seawater, where dissolved Fe^{2+} was partially oxidized to Fe^{3+} hydroxide/oxides in the seawater column. The $\delta^{56}Fe_T$ and $\delta^{56}Fe_{HR}$ signature of the Silikou section primarily depends upon the mixing of Fe^{3+} hydroxide/oxides precipitated from ferruginous water and the syngeneic framboidal pyrite formed within intermittent euxinic conditions. No significant change in Fe geochemical cycling was observed during the late Ediacaran. At the lower part of the slope location, the seawater-like $\delta^{34}S$ value was preserved when sulfate was quantitatively reduced to form diagenetic pyrites during early diagenesis. However, a large S isotope fractionation was observed in the basin location. Subsequently, the S isotope signals of pyrite showed a 30‰ decrease along two investigated sections, which may reflect the enlarged marine sulfate

Table A.1
The iron and sulfur isotopic composition, Fe species data and other geochemical data for our investigated sections.

Samples	Lithology	Depth (m)	$\delta^{57/54}Fe_T$ (‰)	2σ (‰)	$\delta^{56/54}Fe_T$ (‰)	2σ (‰)	$\delta^{56/54}Fe_{HR}$ (‰)	$\delta^{34}S_{PY}$ (‰)	TOC (%)	TS (%)	Fe_T (%)	Al (%)	Fe_T/Al	Fe_{Py} (%)	Fe_{carb} (%)	Fe_{ox} (%)	Fe_{mag} (%)	Fe_{HR} (%)	Fe_{HR}/Fe_T	Fe_{Py}/Fe_{HR}
The slope Yinjiang section																				
E1n-109	Chert	40	0.52	0.16	0.38	0.12	0.38		1.56	0.13	0.28	1.18*	0.24							
Z2l-107	Chert	37	0.38	0.08	0.26	0.06	0.25	8.3	2.24	0.32	0.43	0.58	0.74	0.01	0.04	0.36	0.04	0.44	1.03	0.02
Z2l-104	Chert	32.5	0.58	0.18	0.42	0.10	0.43	18.1	0.78	0.17	0.21	1.59	0.13	0.06	0.03	0.09	0.02	0.20	0.97	0.28
Z2l-102	Chert	29.5	−0.09	0.10	−0.12	0.08	−0.12	4.1			0.46	0.22*	2.09							
Z2l-100	Chert	26.5	0.80	0.09	0.56	0.01	0.56	15.0	0.34	0.41	1.86	1.47	1.27	1.14	0.23	0.55	0.05	1.97	1.06	0.58
Z2l-99	Chert	25	0.77	0.19	0.53	0.03	0.53	13.6	0.68	0.13	0.21	1.55*	0.14	0.01	0.05	0.16	0.02	0.23	1.10	0.06
Z2l-97	Chert	22	0.62	0.16	0.41	0.14	0.47	16.3			0.31	1.21*	0.26	0.12	0.02	0.10	0.02	0.27	0.86	0.46
Z2l-95	Chert	19	1.20	0.14	0.80	0.02	0.84	23.1	1.46	0.56	0.72	6.55	0.11	0.24	0.04	0.30	0.10	0.69	0.95	0.36
Z2l-94	Chert	17.5	0.12	0.07	0.07	0.01	0.07				0.81	2.59*	0.31							
Z2l-93	Chert	16	0.64	0.01	0.44	0.06	0.44	26.4	0.59	0.72	0.75	1.96	0.38	0.60	0.14	0.05	0.02	0.80	1.07	0.74
Z2l-91	Chert	13	0.72	0.18	0.48	0.13	0.48	36.9	0.44	0.43	0.46	1.01*	0.46	0.25	0.02	0.17	0.02	0.47	1.03	0.54
Z2l-90	Chert	11.5	1.60	0.16	1.06	0.10	1.06	32.4	0.97	1.23	1.43	2.46	0.58	0.58	0.09	0.75	0.16	1.58	1.10	0.37
Z2l-88	Chert	8.5	0.65	0.15	0.46	0.15	0.46	33.3	0.59	0.2	0.37	1.59*	0.23	0.05	0.04	0.28	0.04	0.41	1.12	0.13
Z2l-86	Chert	6	1.26	0.04	0.86	0.01	0.86	40.4	0.37	0.15	0.41	1.12	0.37	0.12	0.03	0.29	0.03	0.48	1.16	0.26
Z2l-85	Chert	5	0.58	0.00	0.41	0.05	0.41				0.87	3.66*	0.24							
Z2l-84	Chert	4	0.34	0.17	0.25	0.15	0.25	36.7	0.72	0.42	1.07	3.06	0.35	0.20	0.04	0.73	0.11	1.08	1.01	0.19
Z2l-82	Chert	2						36.0	0.37	0.3	0.84	3.19*	0.26	0.18	0.06	0.53	0.06	0.83	0.98	0.22
Z2l-81	Chert	1							1.37	1.39	1.58	4.06	0.39	0.71	0.14	0.72	0.09	1.66	1.05	0.43
Z2l-80	Chert	0	0.42	0.10	0.28	0.07	0.28				0.92	4.99*	0.18							

Samples	Lithology	Deepth (m)	$\delta^{57/54}Fe_T$ (‰)	2σ (‰)	$\delta^{56/54}Fe_T$ (‰)	2σ (‰)	$\delta^{56/54}Fe_{HR}$ (‰)	$\delta^{34}S_{PY}$ (‰)	TOC (%)	TS (%)	Fe_T (%)	Al (%)	FeT/Al	Fe_{Py} (%)	Fe_{carb} (%)	Fe_{ox} (%)	Fe_{mag} (%)	Fe_{HR} (%)	Fe_{HR}/Fe_T	Fe_{Py}/Fe_{HR}
The basin Slikou section																				
SLK-04	Chert	4	0.28	0.07	0.21	0.03	0.39		0.93	0.005	0.34	0.08	4.25	0.001				0.16	0.47	0.01
SLK-08	Chert	8	0.43	0.08	0.33	0.06	0.70		0.78	0.007	0.33	0.09	3.67	0.002				0.14	0.43	0.01
SLK-12	Chert	12						11.40	0.62	0.018	0.47	0.08	5.92	0.025				0.29	0.61	0.09
SLK-16	Chert	16	0.36	0.06	0.25	0.04	0.41	1.40	0.65	0.1	0.44	0.12	3.67	0.024				0.24	0.55	0.10
SLK-20	Chert	20							0.93	0.063	0.32	0.13	2.52	0.002				0.20	0.63	0.01
SLK-24	Chert	24								0.008	0.27	0.41	0.66	0.003				0.11	0.42	0.03
SLK-31	Chert	31	0.45	0.07	0.29	0.10	0.59		1.09	0.003	0.36	0.18	2.00	0.001				0.16	0.45	0.01
SLK-36	Chert	36	0.43	0.16	0.32	0.09	0.77		0.5	0.015	0.38	0.56	0.68	0.002				0.14	0.37	0.01
SLK-40	Chert	40	0.54	0.10	0.33	0.11	0.47	0.40	0.37	0.004	0.43	0.39	1.10	0.094				0.28	0.66	0.33
SLK-43	Chert	43						−9.30		0.166	0.58	0.55	1.05	0.113				0.32	0.56	0.35
SLK-51	Chert	51						0.60		0.021	0.41	0.95	0.43	0.069				0.26	0.63	0.27
SLK-57	Chert	57	0.57	0.11	0.40	0.04	0.86	1.90	1.25	0.044	0.75	0.49	1.53	0.104				0.32	0.43	0.32
SLK-64	Chert	64	0.10	0.07	0.05	0.04			5.79	0.024	0.43	1.06	0.41							
SLK-74	Chert	74	0.52	0.08	0.38	0.06	0.62	−0.80	3.86	0.035	0.33	0.58	0.57	0.011				0.19	0.58	0.06
SLK-78	Chert	78						−3.40	2.71	0.089	0.83	0.70	1.19	0.101				0.31	0.37	0.32
SLK-82	Chert	82	0.47	0.00	0.34	0.04	0.46	−15.40	1.15	0.364	0.59	0.46	1.28	0.153				0.41	0.70	0.37

Sample	Lithology	m	$\delta^{57/54}Fe_T$	2σ	$\delta^{56/54}Fe_T$	2σ	$\delta^{56/54}Fe_{HR}$	$\delta^{34}S_{PY}$	TOC								
SLK-83	Chert	83						−9.70		0.369	0.32	0.85	0.38	0.001	0.12	0.38	0.01
SLK-87	Chert	87	0.04	0.01	0.03	0.01	−0.03		2.74	0.043	0.48	0.69	0.70	0.001	0.12	0.25	0.01
SLK-90	Chert	90						−12.00		0.019	0.48	0.54	0.89	0.041	0.24	0.50	0.17
SLK-99	Chert	99	0.21	0.08	0.13	0.04			1.99	0.013	0.6	0.50	1.20				
SLK-103	Chert	103	0.41	0.04	0.29	0.03	0.34	−9.10	4.02	0.041	0.52	0.95	0.55	0.234	0.43	0.83	0.54
SLK-107	Chert	107						−7.80		0.469	0.79	0.78	1.01	0.206	0.42	0.53	0.50
SLK-117	Chert	117						−7.30		0.034	0.71	1.12	0.63	0.002	0.19	0.27	0.01
SLK-124	Chert	124	0.10	0.06	0.08	0.00	0.10		0.47	0.049	0.85	7.80	0.11	0.261	0.47	0.55	0.55
SLK-128	Chert	128	0.58	0.04	0.39	0.03			0.44	0.648	0.28	1.95	0.14				
SLK-135	Chert	135	0.24	0.01	0.17	0.04			0.16	0.356	0.47	2.56	0.18				

The reference material	$\delta^{57/54}Fe_T$ (‰)	2σ (‰)	$\delta^{56/54}Fe_T$ (‰)	2σ (‰)	References
BHVO-1	0.17	0.04	0.11	0.02	This study
	0.161	0.012	0.105	0.008	Craddock and Dauphas (2011)
BCR-2	0.12	0.08	0.07	0.06	Our Lab
	0.116	0.08	0.09	0.01	Craddock and Dauphas (2011)
GSR-3	0.23	0.08	0.14	0.04	This study
	0.232	0.028	0.154	0.022	Fan et al. (2014)

The reference material	$\delta^{34}S_{PY}$ (‰)
IAEA S1	−0.23 ± 0.23
IAEA S2	22.7 ± 0.16
IAEA S3	−32.3 ± 0.26

Notes:

Fe concentration and species, Al, TOC, TS and $\delta^{34}S_{PY}$ data of the Silikou section are referenced from Chang et al. (2010a, b, 2012).

Al* data of the Yinjiang section are cited from Fan et al. (2013).

$\delta^{56/54}Fe_{HR}$ values of samples with Fe_{HR}/Fe_T ratios lower than 1.0 were calculated following a simple mass balance equation: $\delta^{56}Fe_T = Fe_{HR}/Fe_T * \delta^{56}Fe_{HR} + (1 - Fe_{HR}/Fe_T) * \delta^{56}Fe_{Detrital}$, where $\delta^{56}Fe_{Detrital}$ is near-zero (~0.05‰, Beard et al., 2003).

reservoir at the basin location and an enhanced diffusion of marine sulfate into the sediments at the slope location. These new data indicate a dominantly ferruginous condition in deep water of the Nanhua basin and no fundamental changes of redox conditions in the two investigated sections of the late Ediacaran.

ACKNOWLEDGMENTS

APPENDIX A

See Table A.1.

REFERENCES

Beard B. L. and Johnson C. M. (2004) Fe isotope variations in the modern and ancient earth and other planetary bodies. *Rev. Mineral. Geochem.* **55**, 319–357.

Beard B. L., Handler R. M., Scherer M. M., Wu L., Czaja A. D., Heimann A. and Johnson C. M. (2010) Iron isotope fractionation between aqueous ferrous iron and goethite. *Earth Planet. Sci. Lett.* **295**, 241–250.

Beard B. L., Johnson C. M., Skulan J. L., Nealson K. H., Cox L. and Sun H. (2003) Application of Fe isotopes to tracing the geochemical and biological cycling of Fe. *Chem. Geol.* **195**, 87–117.

Bullen T. D., White A. F., Childs C. W., Vivit D. V. and Schulz M. S. (2001) Demonstration of significant abiotic iron isotope fractionation in nature. *Geology* **29**, 699–702.

Busigny V., Planavsky N. J., Jézéquel D., Crowe S., Louvat P., Moreau J., Viollier E. and Lyons T. W. (2014) Iron isotopes in an Archean ocean analogue. *Geochim. Cosmochim. Acta* **133**, 443–462.

Butler I. B., Archer C., Vance D., Oldroyd A. and Rickard D. (2005) Fe isotope fractionation on FeS formation in ambient aqueous solution. *Earth Planet. Sci. Lett.* **236**, 430–442.

Canfield D. E. (2001) Biogeochemistry of sulfur isotopes. *Rev. Mineral. Geochem.* **43**, 607–636.

Canfield D. E. and Teske A. (1996) Late Proterozoic rise in atmospheric oxygen concentration inferred from phylogenetic and sulphur isotope studies. *Nature* **382**, 127–132.

Canfield D. E. and Thamdrup B. (1994) The production of 34S-depleted sulfide during bacterial disproportionation of elemental sulfur. *Science* **266**, 1973–1975.

Canfield D. E., Poulton S. W. and Narbonne G. M. (2007) Late-Neoproterozoic deep-ocean oxygenation and the rise of animal life. *Science* **315**, 92–95.

Canfield D. E., Poulton S. W., Knoll A. H., Narbonne G. M., Ross G., Godlberg T. and Strauss H. (2008) Ferruginous conditions dominated later-Neoproterozoic deep-water chemistry. *Science* **321**, 949–952.

Canfield D. E., Farquhar J. and Zerkle A. L. (2010) High isotope fractionations during sulfate reduction in a low-sulfate euxinic ocean analog. *Geology* **38**, 415–418.

Canfield D. E., Raiswell R., Westrich J. T., Reaves C. M. and Berner R. A. (1986) The use of chromium reduction in the analysis of reduced inorganic sulfur in sediments and shales. *Chem. Geol.* **54**, 149–155.

Chang H. J., Chu X. L., Feng L. J. and Huang J. (2009) Framboidal pyrites in cherts of the Laobao Formation, South China: evidence for anoxic deep ocean in the terminal Ediacaran. *Acta Petrologica Sinica* **25**, 1001–1007 (in Chinese with English abstract).

Chang H. J., Chu X. L., Feng L. J. and Huang J. (2010a) Iron speciation in chert from the Laobao Formation, South China: implications for anoxic and ferruginous deep-water conditions. *Chin. Sci. Bull.* **55**, 3189–3196.

Chang H. J., Chu X. L., Feng L. J. and Huang J. (2010b) The major and REE geochemistry of the Silikou chert in Northern Guangxi Province. *Acta Sedimentologica Sinica* **28**, 1098–1107 (in Chinese with English abstract).

Chang H. J., Chu X. L., Feng L. J. and Huang J. (2012) Progressive oxidation of anoxic and ferruginous deep-water during deposition of the terminal Ediacaran Laobao Formation in South China. *Palaeogeogr. Palaeoclimatol. Palaeoecol.* **321–322**, 80–87.

Chen D. Z., Wang J. G., Qing H. R., Yan D. T. and Li R. W. (2009) Hydrothermal venting activities in the Early Cambrian, South China: petrological, geochronological and stable isotopic constraints. *Chem. Geol.* **258**, 168–181.

Chen D. Z., Zhou X. Q., Fu Y., Wang J. G. and Yan D. T. (2015a) New U-Pb zircon ages of the Ediacaran-Cambrian boundary strata in South China. *Terra Nova.* **27**, 62–68.

Chen X., Ling H. F., Vance D., Shields-zhou G. A., Zhu M. Y., Poulton S. W., Och L. M., Jiang S. Y., Li D., Cremonese L. and Archer C. (2015b) Rise to modern levels of ocean oxygenation coincided with the Cambrian radiation of animals. *Nat. Commun.* **6**, 7142. https://doi.org/10.1038/ncomms8142.

Clarkson M. O., Poulton S. W., Guilbaud R. and Wood R. A. (2014) Assessing the utility of Fe/Al and Fe-speciation to record water column redox conditions in carbonate-rich sediments. *Chem. Geol.* **382**, 111–122.

Condon D., Zhu M. Y., Bowring S., Wang W., Yang A. H. and Jin Y. G. (2005) U-Pb ages from the Neoproterozoic Doushantuo formation, China. *Science* **308**, 95–98.

Craddock P. R. and Dauphas N. (2011) Iron and carbon isotope evidence for microbial iron respiration throughout the Archean. *Earth Planet. Sci. Lett.* **303**, 121–132.

Cui H., Kaufman A. J., Xiao S., Peek S., Cao H., Min X., Cai Y., Siegel Z., Liu X. M., Schiffbauer J. D. and Martin A. J. (2016) Environmental context for the terminal Ediacaran biomineralization of animals. *Geobiology* **14**, 344–363.

Czaja A. D., Johnson C. M., Beard B. L., Roden E. E., Li W. and Moorbath S. (2013) Bio-logical Fe oxidation controlled deposition of banded iron formation in the ca. 3770 Ma Isua Supracrustal Belt (West Greenland). *Earth Planet. Sci. Lett.* **363**, 192–203.

Dong L., Shen B., Lee Shu C. T. A. X. J., Peng Y., Sun Y. L., Tang Z. H., Rong H., Lang X. G., Ma H. R., Yang F. and Guo W. (2015) Germanium/silicon of the Ediacaran-Cambrian Laobao chert: Implications for the bedded chert formation and paleoenvironment interpretations. *Geochem. Geophys. Geosyst.* **16**, 751–763.

Duan Y., Severmann S., Anbar A. D., Lyons T. W., Gordon G. W. and Sageman B. B. (2010) Isotopic evidence for Fe cycling and repartitioning in ancient oxygen-deficient settings: examples

from black shales of the mid-to-late Devonian Appalachian basin. *Earth Planet. Sci. Lett.* **290**, 244–253.

Eickmann B., Hofmann A., Wille M., Bui T. H., Wing B. A. and Schoenberg R. (2018) Isotopic evidence for oxygenated mesoarchaean shallow oceans. *Nat. Geosci.* **11**, 133–138.

Fan H. F., Wen H. J., Zhu X. K., Hu R. Z. and Tian S. H. (2013) Hydrothermal activity during Ediacaran-Cambrian transition: Silicon isotopic evidence. *Precambrian Res.* **224**, 23–35.

Fan H. F., Zhu X. K., Wen H. J., Yan B., Li J. and Feng L. J. (2014) Oxygenation of Ediacaran Oceanrecorded by iron isotopes. *Geochim. Cosmochim. Acta* **140**, 80–94.

Fehr M. A., Andersson P. S., Hålenius U., Gustafsson Ö. and Mörth C. M. (2010) Iron enrichments and Fe isotopic compositions of surface sediments from the Gotland Deep, Baltic Sea. *Chem. Geol.* **277**, 310–322.

Fike D. A. and Grotzinger J. P. (2008) A paired sulfate-pyrite δ34S approach to understanding the evolution of the Ediacaran-Cambrian sulfur cycle. *Geochim. Cosmochim. Acta* **72**, 2636–2648.

Fike D. A., Grotzinger J. P., Pratt L. M. and Summons R. E. (2006) Oxidation of the Ediacaran ocean. *Nature* **444**, 744–747.

Guilbaud R., Butler I. B. and Ellam R. M. (2011) Abiotic pyrite formation produces a large Fe isotope fractionation. *Science* **332**, 1548–1551.

Habicht K. S., Gade M., Thamdrup B., Berg P. and Canfield D. E. (2002) Calibration of sulfate levels in the Archean Ocean. *Science* **298**, 2372–2374.

Halverson G. P. and Hurtgen M. T. (2007) Ediacaran growth of the marine sulfate reservoir. *Earth Planet. Sci. Lett.* **263**, 32–44.

Han T. and Fan H. F. (2015) Dynamic evolution of the Ediacaran ocean across the Doushantuo Formation, South China. *Chem. Geol.* **417**, 261–272.

Huang J., Liu J., Zhang Y. N., Chang H. J., Shen Y. A., Huang F. and Qin L. P. (2018) Cr isotopic composition of the Laobao Cherts during the Ediacaran–Cambrian transition in South China. *Chem. Geol.* **482**, 121–130.

Jin C. S., Li C., Algeo T. J., Planavsky N. J., Cui H., Yang X. L., Zhao Y. L., Zhang X. L. and Xie S. C. (2016) A highly redox-heterogeneous ocean in South China during the early Cambrian (∼529–514 Ma): implications for biota-environment co-evolution. *Earth Planet. Sci. Lett.* **441**, 38–51.

Johnson C. M., Skulan J. L., Beard B. L., Sun H., Nealson K. H. and Braterman P. S. (2002) Isotopic fractionation between Fe (III) and Fe(II) in aqueous solutions. *Earth Planet Sci. Lett.* **195**, 141–153.

Johnson C. M., Beard B. L., Beukes N. J., Klein C. and O'Leary J. (2003) Ancient geochemical cy-cling in the Earth as inferred from Fe isotope studies of banded iron formations from the Transvaal Craton. *Contrib. Mineral. Petr.* **144**, 523–547.

Johnson C. M., Beard B. L., Klein C., Beukes N. J. and Roden E. E. (2008) Iron isotopes constrain biologic and abiologic processes in banded Iron formation genesis. *Geochim. Cosmochim. Acta* **72**, 151–169.

Johnston D. T., Poulton S. W., Goldberg T., Sergeev V. N., Podkovyrov V., VorobEva N. G., Bekker A. and Knoll A. H. (2012) Late Ediacaran redox stability and metazoan evolution. *Earth Planet. Sci. Lett.* **335**, 25–35.

Kendall B., Komiya T., Lyons T. W., Bates S. M., Gordon G. W., Romaniello S. J., Jiang G. Q., Creaser R. A., Xiao S. H., McFadden K., Sawaki Y., Tahata M., Shu D. G., Han J., Li Y., Chu X. L. and Anbar A. D. (2015) Uranium and molybdenum isotope evidence for an episode of widespread ocean oxygenation during the late Ediacaran Period. *Geochim. Cosmochim. Acta* **156**, 173–193.

Knoll A. H. and Carroll S. B. (1999) Early animal evolution: emerging views from comparative biology and geology. *Science* **284**, 2129–2137.

Kunzmann M., Gibson T. M., Halverson G. P., Hodgskiss M. S. W., Bui T. H. and Carozza D. A. (2017) Iron isotope biogeochemistry of neoproterozoic marine shales. *Geochim. Cosmochim. Acta* **209**, 85–105.

Kurzweil F., Drost K., Pašava J., Wille M., Taubald H., Schoeckle D. and Schoenberg R. (2015) Coupled sulfur, iron and molybdenum isotope data from black shales of the Teplá-Barrandian unit argue against deep ocean oxygenation during the Ediacaran. *Geochim. Cosmochim. Acta* **171**, 121–142.

Li C., Love G. D., Lyons T. W., Fike D. A., Sessions A. L. and Chu X. L. (2010) A stratified redox model for the Ediacaran ocean. *Science* **328**, 80–83.

Li W., Czaja A. D., Van Kranendonk M. J., Beard B. L., Roden E. E. and Johnson C. M. (2013) An anoxic, Fe(II)-rich, U-poor ocean 3.46 billion years ago. *Geochim. Cosmochim. Acta* **120**, 65–79.

Li C., Planavsky N. J., Shi W., Zhang Z. H., Zhou C. M., Cheng M., Tarhan L. G., Luo G. M. and Xie S. C. (2015) Ediacaran marine redox heterogeneity and early animal ecosystems. *Sci. Rep.* **5**, 17097. https://doi.org/10.1038/srep17097.

Li C., Jin C. S., Planavsky N. J., Algeo T. J., Cheng M., Yang X. L., Zhao Y. L. and Xie S. C. (2017) Coupled oceanic oxygenation and metazoan diversification during the early–middle Cambrian? *Geology* **45**. https://doi.org/10.1130/G39208.1.

Lyons T. W., Anbar A. D., Severmann S., Scott C. and Gill B. C. (2009) Tracking euxinia in the ancient ocean: a multiproxy perspective and proterozoic case study. *Annu. Rev. Earth Planet. Sci.* **37**, 507–534.

Lyons T. W., Planavsky N. J., Reinhard C. and Raiswell R. (2012) Revisiting iron-based paleoredox proxies in light of diverse primary and secondary controls and overprints: a story of cautious optimism. Abstract No. B11G-05, Fall Meeting, AGU, San Francisco, Calif.

Marin-Carbonne J., Rollion-Bard C., Bekker A., Rouxel O., Agangi A. and Cavalazzi B., et al. (2014) Coupled Fe and S isotope variations in pyrite nodules from archean shale. *Earth Planet. Sci. Lett.* **392**, 67–79.

Nishizawa M., Yamamoto H., Ueno Y., Tsuruoka S., Shibuya T., Sawaki Y., Yamamoto S., Kon Y., Kitajima K., Komiya T., Maruyama S. and Hirata T. (2010) Grain-scale iron isotopic distribution of pyrite from Precambrian shallow marine carbonate revealed by a femtosecond laser ablation multicollector ICP-MS technique: possible proxy for the redox state of ancient seawater. *Geochim. Cosmochim. Acta* **74**, 2760–2778.

Poulton S. W. and Canfield D. E. (2005) Development of a sequential extraction procedure for iron: implications for iron partitioning in continentally derived particulates. *Chem. Geol.* **214**, 209–221.

Poulton S. W. and Raiswell R. (2002) The low-temperature geochemical cycle of iron: from continental fluxes to marine sediment deposition. *Am. J. Sci.* **302**, 774–805.

Raiswell R., Buckley F., Berner R. A. and Anderson T. F. (1988) Degree of pyritization of iron as a paleoenvironmental indicator of bottom-water oxygenation. *J. Sediment. Res.* **58**, 812–819.

Raiswell R., Newton R. and Wignall P. B. (2001) An indicator of water-column anoxia: resolution of biofacies variations in the Kimmeridge clay (Upper Jurassic, U. K.). *J. Sediment. Res.* **71**, 286–294.

Ries J. B., Fike D. A., Pratt L. M., Lyons T. W. and Grotzinger J. P. (2009) Superheavy pyrite ($\delta^{34}S_{pyr}>\delta^{34}S_{CAS}$) in the terminal Proterozoic Nama Group, southern Namibia: a consequence of low seawater sulfate at the dawn of animal life. *Geology* **37**, 743–746.

Sahoo S. K., Planavsky N. J., Kendall B., Wang X. Q., Shi X. Y., Scott C., Anbar A. D., Lyons T. W. and Jiang G. Q. (2012) Ocean oxygenation in the wake of the Marinoan glaciation. *Nature* **489**, 546–549.

Sahoo S. K., Planavsky N. J., Jiang G., Kendall B., Owens J. D., Wang X. and Lyons T. W. (2016) Oceanic oxygenation events in the anoxic Ediacaran ocean. *Geobiology* **14**, 457–468.

Satkoski A. M., Beukes N. J., Li W., Beard B. L. and Johnson C. M. (2015) A redox-stratified ocean 3.2 billion years ago. *Earth Planet. Sci. Lett.* **430**, 43–53.

Sawaki Y., Tahata M., Komiya T., Hirata T., Han J. and Shu D. (2018) Redox history of the three gorges region during the Ediacaran and early Cambrian as indicated by the Fe isotope. *Geosci. Front.* **9**, 155–172.

Scholz F., Severmann S., McManus J. and Hensen C. (2014a) Beyond the Black Sea paradigm: the sedimentary fingerprint of an open-marine iron shuttle. *Geochim. Cosmochim. Acta* **127**, 368–380.

Scholz F., Severmann S., McManus J., Noffke A., Lomnitz U. and Hensen C. (2014b) On the isotope composition of reactive iron in marine sediments: Redox shuttle versus early diagenesis. *Chem. Geol.* **389**, 48–59.

Scott C., Lyons T. W., Bekker A., Shen Y., Poulton S. W. and Chu X. L. (2008) Tracing the stepwise oxygenation of the proterozoic ocean. *Nature* **452**, 456–460.

Severmann S., Johnson C. M., Beard B. L. and McManus J. (2006) The effect of early diagenesis on the Fe isotope compositions of porewaters and authigenic minerals in continental margin sediments. *Geochim. Cosmochim. Acta* **70**, 2006–2022.

Severmann S., Lyons T. W., Anbar A., McManus J. and Gordon G. (2008) Modern iron isotope perspective on the benthic iron shuttle and the redox evolution of ancient oceans. *Geology* **36**, 487–490.

Shen Y., Canfield D. E. and Knoll A. H. (2002) Middle Proterozoic ocean chemistry: evidence from the McArthur basin, Northern Australia. *Am. J. Sci.* **302**, 81–109.

Shen Y., Knoll A. H. and Walter M. R. (2003) Evidence for low sulphate and anoxia in a mid-Proterozoic marine basin. *Nature* **423**, 632–635.

Sperling E. A., Knoll A. H. and Girguis P. R. (2015) The ecological physiology of Earth's second oxygen revolution. *Annu. Rev. Ecol. Evol. Syst.* **46**, 215–235.

Tang S. H., Zhu X. K., Cai J. J., Li S. Z., He X. X. and Wang J. H. (2006) Chromatographic separation of Cu, Fe and Zn using AGMP-1 anion exchange resin for isotope determination by MC-ICPMS. *Rock Mineral Anal.* **25**, 11–14.

Wang J. and Li Z. X. (2003) History of Neoproterozoic rift basins in South China: implications for Rodinia break-up. *Precambrian Res.* **122**, 141–158.

Wang J. G., Chen D. Z., Yan D. T., Wei H. Y. and Xiang L. (2012) Evolution from an anoxic to oxic deep ocean during the Ediacaran-Cambrian transition and implications for bioradiation. *Chem. Geol.* **306–307**, 129–138.

Welch S. A., Beard B. L., Johnson C. M. and Braterman P. S. (2003) Kinetic and equilibrium Fe isotope fractionation between aqueous Fe and Fe(III). *Geochim. Cosmochim. Acta* **67**, 4231–4250.

Wen H. J., Fan H. F., Zhang Y. X., Cloquet C. and Carignan J. (2015) Reconstruction of early Cambrian ocean chemistry from Mo isotopes. *Geochim. Cosmochim. Acta* **164**, 1–16.

Wignall P. B. and Newton R. (1998) Pyrite framboid diameter as a measure of oxygen deficiency in ancient mudrocks. *Am. J. Sci.* **298**, 537–552.

Wilkin R. T., Barnes H. L. and Brantley S. L. (1996) The size distribution of framboidal pyrite in modern sediments: an indicator of redox conditions. *Geochim. Cosmochim. Acta* **60**, 3897–3912.

Wu L. L., Druschel G., Findlay A., Beard B. L. and Johnson C. M. (2012) Experimental determination of iron isotope fractionations among–fesaq–mackinawite at low temperatures: implications for the rock record. *Geochim. Cosmochim. Acta* **89**, 46–61.

Xiang L., Schoepfer S. D., Shen S. Z., Cao C. Q. and Zhang H. (2017) Evolution of oceanic molybdenum and uranium reservoir size around the Ediacaran–Cambrian transition: evidence from western Zhejiang, South China. *Earth Planet. Sci. Lett.* **464**, 84–94.

Xiao S. H., Schiffbauer J. D., McFadden K. A. and Hunter J. (2010) Petrographic and SIMS pyrite sulfur isotope analyses of Ediacaran chert nodules: implications for microbial processes in pyrite rim formation, silicification, and exceptional fossil preservation. *Earth Planet. Sci. Lett.* **297**, 481–495.

Yang C., Zhu M. Y., Condon D. J. and Li X. H. (2017) Geochronological constraints on stratigraphic correlation and oceanic oxygenation in Ediacaran-Cambrian transition in South China. *J. Asian Earth Sci.* **140**, 75–81.

Yoshiya K., Nishizawa M., Sawaki Y., Ueno Y., Komiya T., Yamada K., Yoshida N., Hirata T., Wada H. and Maruyama S. (2012) In situ iron isotope analyses of pyrite and organic carbon isotope ratios in the Fortescue Group: metabolic variations of a Late Archean ecosystem. *Precambrian Res.* **212–213**, 169–193.

Zhang F. F., Zhu X. K., Yan B., Kendall B., Peng X., Li J., Algeo T. J. and Stephen R. (2015) Oxygenation of a Cryogenian Ocean (Nanhua basin, South China) revealed by pyrite Fe isotope compositions. *Earth Planet. Sci. Lett.* **429**, 11–19.

Zhao X. M., Zhang H. F., Zhu X. K., Tang S. H. and Yan B. (2012) Iron isotope evidence for multistage melt–peridotite interactions in the lithospheric mantle of eastern China. *Chem. Geol.* **292–293**, 127–139.

Zhu X. K., Guo Y., Williams R. J. P., O'Nions R. K., Matthews A. and Belshaw N. S., et al. (2002) Mass fractionation processes of transition metal isotopes. *Earth Planet. Sci. Lett.* **200**, 47–62.

Zhu M. Y., Strauss H. and Shields G. A. (2007) From snowball earth to the Cambrian bioradiation: calibration of Ediacaran-Cambrian earth history in South China. *Palaeogeogr. Palaeoclimatol. Palaeoecol.* **254**, 1–6.

Zhu X. K., Li Z. H., Zhao X. M., Tang S. H., He X. X. and Nick S. (2008) High precision measurements of Fe isotopes using MC-ICP-MS and Fe isotope compositions of geological reference materials. *Acta Petrologica et Mineralogica* **27**, 263–272 (in Chinese with English abstract).

Zhu R. X., Li X. H., Hou X. G., Pan Y. X., Wang F., Deng C. L. and He H. Y. (2009) SIMS U-Pb zircon age of a tuff layer in the Meishucun section, Yunnan, southwest China: constraint on the age of the Precambrian-Cambrian boundary. *Sci. China, Ser. D Earth Sci.* **52**, 1385–1392.

Associate editor: Timothy Lyons